

Differential (2+1) jet event rates and determination of α_s in deep inelastic scattering at HERA

H1 Collaboration

C. Adloff³⁴, M. Anderson²², V. Andreev²⁵, B. Andrieu²⁸, V. Arkadov³⁵, I. Ayyaz²⁹, A. Babaev²⁴, J. Bähr³⁵, J. Bán¹⁷, P. Baranov²⁵, E. Barrelet²⁹, R. Barschke¹¹, W. Bartel¹¹, U. Bassler²⁹, P. Bate²², M. Beck¹³, A. Beglarian^{11,40}, O. Behnke¹¹, H.-J. Behrend¹¹, C. Beier¹⁵, A. Belousov²⁵, Ch. Berger¹, G. Bernardi²⁹, G. Bertrand-Coremans⁴, P. Biddulph²², J.C. Bizot²⁷, K. Borras⁸, V. Boudry²⁸, A. Braemer¹⁴, W. Braunschweig¹, V. Brisson²⁷, D.P. Brown²², W. Brückner¹³, P. Bruel²⁸, D. Bruncko¹⁷, J. Bürger¹¹, F.W. Büsler¹², A. Buniatian³², S. Burke¹⁸, G. Buschhorn²⁶, D. Calvet²³, A.J. Campbell¹¹, T. Carli²⁶, E. Chabert²³, M. Charlet⁴, D. Clarke⁵, B. Clerbaux⁴, S. Cocks¹⁹, J.G. Contreras⁸, C. Cormack¹⁹, J.A. Coughlan⁵, M.-C. Cousinou²³, B.E. Cox²², G. Cozzika⁹, J. Cvach³⁰, J.B. Dainton¹⁹, W.D. Dau¹⁶, K. Daum³⁹, M. David⁹, A. De Roeck¹¹, E.A. De Wolf⁴, B. Delcourt²⁷, C. Diaconu²³, M. Dirkmann⁸, P. Dixon²⁰, W. Dlugosz⁷, K.T. Donovan²⁰, J.D. Dowell³, A. Drutskoi²⁴, J. Ebert³⁴, G. Eckerlin¹¹, D. Eckstein³⁵, V. Efremenko²⁴, S. Egli³⁷, R. Eichler³⁶, F. Eisele¹⁴, E. Eisenhandler²⁰, E. Elsen¹¹, M. Enzenberger²⁶, M. Erdmann^{14,41,f}, A.B. Fahr¹², L. Favart⁴, A. Fedotov²⁴, R. Felst¹¹, J. Feltesse⁹, J. Ferencei¹⁷, F. Ferrarotto³², K. Flamm¹¹, M. Fleischer⁸, G. Flüge², A. Fomenko²⁵, J. Formánek³¹, J.M. Foster²², G. Franke¹¹, E. Gabathuler¹⁹, K. Gabathuler³³, F. Gaede²⁶, J. Garvey³, J. Gayler¹¹, M. Gebauer³⁵, R. Gerhards¹¹, S. Ghazaryan^{11,40}, A. Glazov³⁵, L. Goerlich⁶, N. Gogitidze²⁵, M. Goldberg²⁹, I. Gorelov²⁴, C. Grab³⁶, H. Grässler², T. Greenshaw¹⁹, R.K. Griffiths²⁰, G. Grindhammer²⁶, C. Gruber¹⁶, T. Hadig¹, D. Haidt¹¹, L. Hajduk⁶, T. Haller¹³, M. Hampel¹, V. Haustein³⁴, W.J. Haynes⁵, B. Heinemann¹¹, G. Heinzelmann¹², R.C.W. Henderson¹⁸, S. Hengstmann³⁷, H. Henschel³⁵, R. Heremans⁴, I. Herynek³⁰, K. Hewitt³, K.H. Hiller³⁵, C.D. Hilton²², J. Hladký³⁰, D. Hoffmann¹¹, T. Holtom¹⁹, R. Horisberger³³, V.L. Hudgson³, S. Hurling¹¹, M. Ibbotson²², Ç. İlsever⁸, H. Itterbeck¹, M. Jacquet²⁷, M. Jaffre²⁷, D.M. Jansen¹³, L. Jönsson²¹, D.P. Johnson⁴, H. Jung²¹, M. Kander¹¹, D. Kant²⁰, U. Kathage¹⁶, J. Katzy¹¹, H.H. Kaufmann³⁵, O. Kaufmann¹⁴, M. Kausch¹¹, I.R. Kenyon³, S. Kermiche²³, C. Keuker¹, C. Kiesling²⁶, M. Klein³⁵, C. Kleinwort¹¹, G. Knies¹¹, J.H. Köhne²⁶, H. Kolanoski³⁸, S.D. Kolya²², V. Korbel¹¹, P. Kostka³⁵, S.K. Kotelnikov²⁵, T. Krämerkämper⁸, M.W. Krasny²⁹, H. Krehbiel¹¹, D. Krücker²⁶, A. Küpper³⁴, H. Küster²¹, M. Kuhlen²⁶, T. Kurča³⁵, B. Laforge⁹, R. Lahmann¹¹, M.P.J. Landon²⁰, W. Lange³⁵, U. Langenegger³⁶, A. Lebedev²⁵, M. Lehmann¹⁶, F. Lehner¹¹, V. Lemaître¹¹, S. Levonian¹¹, M. Lindstroem²¹, B. List¹¹, G. Lobo²⁷, V. Lubimov²⁴, D. Lüke^{8,11}, L. Lytkin¹³, N. Magnussen³⁴, H. Mahlke-Krüger¹¹, E. Malinovski²⁵, R. Maraček¹⁷, P. Marage⁴, J. Marks¹⁴, R. Marshall²², G. Martin¹², R. Martin¹⁹, H.-U. Martyn¹, J. Martyniak⁶, S.J. Maxfield¹⁹, S.J. McMahon¹⁹, T.R. McMahon¹⁹, A. Mehta⁵, K. Meier¹⁵, P. Merkel¹¹, F. Metlica¹³, A. Meyer¹², A. Meyer¹¹, H. Meyer³⁴, J. Meyer¹¹, P.-O. Meyer², A. Migliori²⁸, S. Mikocki⁶, D. Milstead¹⁹, J. Moeck²⁶, R. Mohr²⁶, S. Mohrdieck¹², F. Moreau²⁸, J.V. Morris⁵, E. Mroczko⁶, D. Müller³⁷, K. Müller¹¹, P. Murín¹⁷, V. Nagovizin²⁴, B. Naroska¹², Th. Naumann³⁵, I. Négri²³, P.R. Newman³, D. Newton¹⁸, H.K. Nguyen²⁹, T.C. Nicholls¹¹, F. Niebergall¹², C. Niebuhr¹¹, Ch. Niedzballa¹, H. Niggli³⁶, O. Nix¹⁵, G. Nowak⁶, T. Nunnemann¹³, H. Oberlack²⁶, J.E. Olsson¹¹, D. Ozerov²⁴, P. Palmen², E. Panaro¹¹, A. Panitch⁴, C. Pascaud²⁷, S. Passaggio³⁶, G.D. Patel¹⁹, H. Pawletta², E. Peppel³⁵, E. Perez⁹, J.P. Phillips¹⁹, A. Pieuchot¹¹, D. Pitzl³⁶, R. Pöschl⁸, G. Pope⁷, B. Povh¹³, K. Rabbertz¹, P. Reimer³⁰, B. Reisert²⁶, H. Rick¹¹, S. Riess¹², E. Rizvi¹¹, P. Robmann³⁷, R. Roosen⁴, K. Rosenbauer¹, A. Rostovtsev^{24,11}, F. Rouse⁷, C. Royon⁹, S. Rusakov²⁵, K. Rybicki⁶, D.P.C. Sankey⁵, P. Schacht²⁶, J. Scheins¹, S. Schiek¹¹, S. Schleich¹⁵, P. Schleper¹⁴, D. Schmidt³⁴, G. Schmidt¹¹, L. Schoeffel⁹, V. Schröder¹¹, H.-C. Schultz-Coulon¹¹, B. Schwab¹⁴, F. Sefkow³⁷, A. Semenov²⁴, V. Shekelyan²⁶, I. Sheviakov²⁵, L.N. Shtarkov²⁵, G. Siegmon¹⁶, U. Siewert¹⁶, Y. Sirois²⁸, I.O. Skillicorn¹⁰, T. Sloan¹⁸, P. Smirnov²⁵, M. Smith¹⁹, V. Solochenko²⁴, Y. Soloviev²⁵, A. Specka²⁸, J. Spiekermann⁸, H. Spitzer¹², F. Squinabol²⁷, P. Steffen¹¹, R. Steinberg², J. Steinhart¹², B. Stella³², A. Stellberger¹⁵, J. Stiewe¹⁵, U. Straumann¹⁴, W. Strucziński², J.P. Sutton³, M. Swart¹⁵, S. Tapprogge¹⁵, M. Taševský³¹, V. Tchernyshov²⁴, S. Tchetelnitski²⁴, J. Theissen², G. Thompson²⁰, P.D. Thompson³, N. Tobien¹¹, R. Todenhagen¹³, P. Truöl³⁷, G. Tsipolitis³⁶, J. Turnau⁶, E. Tzamariudaki¹¹, S. Udluft²⁶, A. Usik²⁵, S. Valkár³¹, A. Valkárová³¹, C. Vallée²³, P. Van Esch⁴, P. Van Mechelen⁴, Y. Vazdik²⁵, G. Villet⁹, K. Wacker⁸, R. Wallny¹⁴, T. Walter³⁷, B. Waugh²², G. Weber¹², M. Weber¹⁵, D. Wegener⁸, A. Wegner²⁶, T. Wengler¹⁴, M. Werner¹⁴, L.R. West³, S. Wiesand³⁴, T. Wilksen¹¹, S. Willard⁷, M. Winde³⁵, G.-G. Winter¹¹, C. Wittke¹², E. Wittmann¹³, M. Wobisch², H. Wollatz¹¹, E. Wünsch¹¹, J. Žáček³¹, J. Zálešák³¹, Z. Zhang²⁷, A. Zhokin²⁴, P. Zini²⁹, F. Zomer²⁷, J. Zembery⁹, M. zurNedden³⁷

- ¹ I. Physikalisches Institut der RWTH, Aachen, Germany^a
² III. Physikalisches Institut der RWTH, Aachen, Germany^a
³ School of Physics and Space Research, University of Birmingham, Birmingham, UK^b
⁴ Inter-University Institute for High Energies ULB-VUB, Brussels; Universitaire Instelling Antwerpen, Wilrijk; Belgium^c
⁵ Rutherford Appleton Laboratory, Chilton, Didcot, UK^b
⁶ Institute for Nuclear Physics, Cracow, Poland^d
⁷ Physics Department and IIRPA, University of California, Davis, California, USA^e
⁸ Institut für Physik, Universität Dortmund, Dortmund, Germany^a
⁹ DSM/DAPNIA, CEA/Saclay, Gif-sur-Yvette, France
¹⁰ Department of Physics and Astronomy, University of Glasgow, Glasgow, UK^b
¹¹ DESY, Hamburg, Germany^a
¹² II. Institut für Experimentalphysik, Universität Hamburg, Hamburg, Germany^a
¹³ Max-Planck-Institut für Kernphysik, Heidelberg, Germany^a
¹⁴ Physikalisches Institut, Universität Heidelberg, Heidelberg, Germany^a
¹⁵ Institut für Hochenergiephysik, Universität Heidelberg, Heidelberg, Germany^a
¹⁶ Institut für experimentelle und angewandte Physik, Universität Kiel, Kiel, Germany^a
¹⁷ Institute of Experimental Physics, Slovak Academy of Sciences, Košice, Slovak Republic^{f,j}
¹⁸ School of Physics and Chemistry, University of Lancaster, Lancaster, UK^b
¹⁹ Department of Physics, University of Liverpool, Liverpool, UK^b
²⁰ Queen Mary and Westfield College, London, UK^b
²¹ Physics Department, University of Lund, Lund, Sweden^g
²² Department of Physics and Astronomy, University of Manchester, Manchester, UK^b
²³ CPPM, Université d'Aix-Marseille II, IN2P3-CNRS, Marseille, France
²⁴ Institute for Theoretical and Experimental Physics, Moscow, Russia
²⁵ Lebedev Physical Institute, Moscow, Russia^{f,k}
²⁶ Max-Planck-Institut für Physik, München, Germany^a
²⁷ LAL, Université de Paris-Sud, IN2P3-CNRS, Orsay, France
²⁸ LPNHE, Ecole Polytechnique, IN2P3-CNRS, Palaiseau, France
²⁹ LPNHE, Universités Paris VI and VII, IN2P3-CNRS, Paris, France
³⁰ Institute of Physics, Academy of Sciences of the Czech Republic, Praha, Czech Republic^{f,h}
³¹ Nuclear Center, Charles University, Praha, Czech Republic^{f,h}
³² INFN Roma 1 and Dipartimento di Fisica, Università Roma 3, Roma, Italy
³³ Paul Scherrer Institut, Villigen, Switzerland
³⁴ Fachbereich Physik, Bergische Universität Gesamthochschule Wuppertal, Wuppertal, Germany^a
³⁵ DESY, Institut für Hochenergiephysik, Zeuthen, Germany^a
³⁶ Institut für Teilchenphysik, ETH, Zürich, Switzerlandⁱ
³⁷ Physik-Institut der Universität Zürich, Zürich, Switzerlandⁱ
³⁸ Institut für Physik, Humboldt-Universität, Berlin, Germany^a
³⁹ Rechenzentrum, Bergische Universität Gesamthochschule Wuppertal, Wuppertal, Germany^a
⁴⁰ Vistor from Yerevan Physics Institute, Armenia
⁴¹ Institut für Experimentelle Kernphysik, Universität Karlsruhe, Karlsruhe, Germany

Received: 25 June 1998 / Published online: 5 October 1998

Abstract. Events with a (2+1) jet topology in deep-inelastic scattering at HERA are studied in the kinematic range $200 < Q^2 < 10\,000 \text{ GeV}^2$. The rate of (2+1) jet events has been determined with the modified JADE jet algorithm as a function of the jet resolution parameter and is compared with the predictions of Monte Carlo models. In addition, the event rate is corrected for both hadronization and detector effects and is compared with next-to-leading order QCD calculations. A value of the strong coupling constant of $\alpha_s(M_Z^2) = 0.118 \pm 0.002$ (*stat.*) $^{+0.007}_{-0.008}$ (*sys.*) $^{+0.007}_{-0.006}$ (*theory*) is extracted. The systematic error includes uncertainties in the calorimeter energy calibration, in the description of the data by current Monte Carlo models, and in the knowledge of the parton densities. The theoretical error is dominated by the renormalization scale ambiguity.

^a Supported by the Bundesministerium für Bildung, Wissenschaft, Forschung und Technologie, FRG, under contract numbers 7AC17P, 7AC47P, 7DO55P, 7HH17I, 7HH27P, 7HD17P, 7HD27P, 7KI17I, 6MP17I and 7WT87P

^b Supported by the UK Particle Physics and Astronomy Research Council, and formerly by the UK Science and Engineer-

ing Research Council

^c Supported by FNRS-NFWO, IISN-IKW

^d Partially supported by the Polish State Committee for Scientific Research, grant no. 115/E-343/SPUB/P03/002/97 and grant no. 2P03B 055 13

^e Supported in part by US DOE grant DE F603 91ER40674

1 Introduction

We present a study of events with a (2+1) jet topology and determine the strong coupling constant, α_s , using neutral current deep-inelastic scattering (DIS) events recorded with the H1 detector at the ep collider HERA in 1994 and 1995. In this period HERA was operated with positron and proton beams of 27.5 and 820 GeV energy, respectively, corresponding to a centre-of-mass energy of $\sqrt{s} = 300$ GeV.

In the Quark-Parton-Model, neutral current DIS corresponds to the interaction of a virtual photon or Z^0 boson with a quark in the proton. The interaction can be characterized by the two independent variables Q^2 and x where Q^2 is the absolute value of the virtual boson 4-momentum squared and x is related to the fraction of the proton momentum carried by the struck quark. Experimentally, events with a (1+1) jet topology are observed. The notation ‘+1’ refers to the proton remnant jet. QCD corrections in $O(\alpha_s)$, namely QCD-Compton scattering ($\gamma q \rightarrow qg$) and Boson-Gluon-Fusion ($\gamma g \rightarrow q\bar{q}$), lead to (2+1) parton final states. Due to the high centre-of-mass energy at HERA, multi-jet structures have been observed clearly [1], and quantitative tests of QCD and the determination of the strong coupling constant α_s are made possible.

Previous jet analyses and determinations of α_s at HERA were based on the measurement of $R_{2+1}(Q^2)$, the (2+1) jet event rate as a function of Q^2 [2]. The jets were found by applying the modified JADE jet algorithm [3] in the laboratory frame for a fixed value of the jet resolution parameter. In particular, the measurement of $R_{2+1}(Q^2)$ allows the dependence of α_s on the scale Q^2 to be studied in a single experiment. In this analysis a complementary approach is adopted. We take events in the range $200 < Q^2 < 10\,000$ GeV² and then cluster measured calorimeter energy depositions with the modified JADE jet algorithm until (2+1) jets remain. The minimum mass squared of any pair of the (2+1) jet four-vectors, scaled by the hadronic energy squared W^2 , is the variable y_2 , which we study. For a clear (1+1) jet event a small value of y_2 is expected whereas any event with a larger jet multiplicity must result in a large value.

This is the first measurement of differential jet event rates at HERA [4]. The presence of a strongly interacting particle in the initial state gives rise to considerable differences from the situation in e^+e^- annihilation, where differential jet event rates have been studied in much detail [5]. The proton remnant, the initial state QCD radiation, the large momenta of the produced jets in the direction of the incoming proton, and finally the uncertainties in the

knowledge of the parton content of the proton complicate the measurement. The study of the same observable in processes as different as e^+e^- annihilation and ep scattering, however, may lead to improved understanding of systematic uncertainties in the determination of α_s from hadronic final states and provides an important test of QCD.

The analysis consists of the following steps. After the data selection, the accuracy with which the data are described by the colour dipole Monte Carlo model ARIADNE [6] and the leading-logarithm parton shower model LEPTO [7] is studied. The rate of (2+1) jet events is corrected for detector acceptance, resolution and inefficiencies as well as for hadronization effects. A sophisticated correction procedure is used that takes migration effects into account. Next, the parton jet distributions of these models are compared qualitatively with next-to-leading order (NLO) calculations available in the form of the programs MEPJET [8] and DISENT [9], in order to verify that a jet phase space region has been selected in which the NLO calculations can be expected to be a good approximation to the data. Finally, the NLO calculations are fitted to the corrected data as a function of α_s , and the systematic uncertainties are evaluated.

2 The H1 detector

A detailed description of the H1 detector can be found in [10]. The components most relevant for this analysis are the central tracking system, the liquid argon calorimeter, the backward electromagnetic calorimeter, and the instrumented iron return yoke.

The central tracking system consists of several inner and outer drift and proportional chambers. It is used in this analysis to determine the ep collision point and to aid the identification of the scattered positron. The tracking system is surrounded by a large liquid argon sampling calorimeter covering a polar angle range of $4^\circ < \theta < 154^\circ$. The polar angle θ is measured with respect to the incoming proton beam which is defined to point in the $+z$ direction. The electromagnetic and hadronic sections of the liquid argon calorimeter correspond in total to a depth of 4.5 to 8 interaction lengths. The energy resolution of the liquid argon calorimeter for electrons and hadronic showers is $\sigma/E = 12\%/\sqrt{E(\text{GeV})} \oplus 1\%$ and $\sigma/E = 50\%/\sqrt{E(\text{GeV})} \oplus 2\%$, respectively [11]. The absolute energy scale for hadronic energy depositions is known to better than 4%, and that for electromagnetic energy depositions to better than 3%.

Since 1995 the backward region of the H1 detector has been equipped with a drift chamber and a lead/scintillating-fibre calorimeter. Its main purpose is the detection of electrons at small scattering angles. In addition, the timing information it provides allows efficient discrimination against out-of-time proton beam related background events at early trigger levels. Before 1995 the backward region was instrumented with a multi-wire proportional chamber, a lead/scintillator electromagnetic calorimeter, and a scintillator array for timing measurements.

^f Supported by the Deutsche Forschungsgemeinschaft

^g Supported by the Swedish Natural Science Research Council

^h Supported by GA ĆR grant no. 202/96/0214, GA AV ĆR grant no. A1010619 and GA UK grant no. 177

ⁱ Supported by the Swiss National Science Foundation

^j Supported by VEGA SR grant no. 2/1325/96

^k Supported by Russian Foundation for Basic Researches grant no. 96-02-00019

Outside the calorimeters a large superconducting solenoid provides a magnetic field of 1.15 Tesla. The instrumented iron return yoke identifies energetic muons and detects leakage of hadronic showers.

3 Event and cluster selection

Neutral current DIS events are selected using the following criteria. We require a scattered positron candidate to be detected within $\theta_e < 150^\circ$ so that it is well contained within the acceptance of the liquid argon calorimeter. A cluster of contiguous energy depositions in the calorimeter is identified as a positron candidate if its energy deposition in the electromagnetic calorimeter section exceeds 80% of the cluster energy and if its lateral and longitudinal profiles are compatible with those of an electromagnetic shower [12]. In addition, its position must be matched to a reconstructed track to better than 1.7° in polar angle and to better than 6° in azimuthal angle. The Q^2 range is restricted to $200 < Q^2 < 10\,000 \text{ GeV}^2$ where Q^2 is determined from the scattered positron energy and polar angle. The cut $Q^2 > 200 \text{ GeV}^2$ offers several advantages: hadronic final state particles are better contained in the detector since they must balance the transverse momentum of the scattered positron, which is detected in the liquid argon calorimeter at large Q^2 ; the range of x is implicitly restricted to larger values of x where the parton density of the proton is better known and where initial-state QCD radiation beyond NLO is suppressed.

The measured z coordinate of the primary event vertex is required to be within a distance of 30 cm from the nominal ep collision point. The time-of-flight information of the backward scintillator array is required not to be inconsistent with impact times of particles originating from the ep collision point. Both cuts strongly reduce proton beam-related background events.

The inelasticity $y = Q^2/sx$, calculated from the scattered positron energy and polar angle, is required to be smaller than 0.7. This cut corresponds to a polar angle dependent minimum positron energy requirement to suppress background from misidentified photoproduction events and to reduce the influence of QED radiation. The remaining effects of initial and final state QED radiation were studied with DJANGO [13]. They were found to be small and are neglected in the following. Photoproduction and beam-related background events are further suppressed by requiring $30 < E - P_z < 70 \text{ GeV}$ where E and P_z are the summed energy and longitudinal momentum components of all reconstructed clusters, each assumed to be massless. For NC DIS events $E - P_z$ is ideally expected to be 55 GeV, corresponding to twice the positron beam energy. The invariant mass squared of the hadronic final state, W_{da}^2 , as calculated using the double angle method [14] is required to exceed $5\,000 \text{ GeV}^2$ to ensure a substantial hadronic activity for jet production. In addition, we reject events where cosmic muons or beam halo muons crossing the detector are identified [15].

The events recorded were triggered by the electron trigger of the liquid argon calorimeter. The above cuts

imply that the energy of the scattered positron always exceeds 10 GeV. The average trigger efficiency for the selected data sample was found to be larger than 99% and is independent of the hadronic final state.

With these cuts we obtain a sample of 11 192 deep-inelastic scattering events corresponding to an integrated luminosity of 7 pb^{-1} . The remaining background from beam-gas collision, photoproduction, cosmic muon or halo muon events in this sample is negligible. In particular, the fraction of photoproduction events is estimated to be less than 0.5%. The fraction of diffractive events [16], defined as events with a calorimeter energy deposition of less than 0.5 GeV in a cone of 15° around the beam direction, is of the order of 1%. After the application of the jet algorithm, further cuts are applied to select a subsample enriched with (2+1) jet events.

In this analysis, hadronic jets are reconstructed from the energy depositions in the liquid argon calorimeter and the instrumented iron. Clusters that are not well measured or that are not related to the hadronic final state are rejected by the following quality cuts: the polar angle, θ_{clus} , of a cluster is required to satisfy $\theta_{clus} > 7^\circ$ to select clusters that are well within the geometrical acceptance of the liquid argon calorimeter, and energy depositions in the backward electromagnetic calorimeter are discarded since this has limited containment for hadrons. Further requirements of less importance are: the energy fraction leaking into the instrumented iron is required to not exceed 40%; hadronic clusters must be separated from the positron candidate by an angle greater than 10° ; clusters with an angle of larger than 50° with respect to their closest neighbouring cluster are rejected. This latter cut is imposed to decrease the sensitivity to isolated noise contributions or to photons radiated from the scattered positron. After these selections the average number of accepted clusters per event is 37.8.

4 Jet algorithms and jet event rate definition

The jets in a given event are found using the JADE jet algorithm [3]. The jet algorithm is applied in the laboratory frame to the clusters of the liquid argon calorimeter and the instrumented iron satisfying the cuts given in Sect. 3. The algorithm is modified compared to the version used in e^+e^- -annihilation in two respects: (a) the cluster that is attributed to the scattered positron is removed; (b) a massless four-vector is determined and is treated as an additional cluster by the jet algorithm to account for the longitudinal component of the momentum carried by the proton remnant particles escaping through the beam pipe.

The jet algorithm calculates the scaled quantity m_{ij}^2/W^2 of pairs of clusters or ‘proto’ jets i, j , where W^2 is the total invariant mass squared of all clusters entering the jet algorithm. The definition of m_{ij}^2 is taken to be $2E_i E_j (1 - \cos \theta_{ij})$. Here E_i and E_j are the energies of the clusters i and j , and θ_{ij} is the angle between them.

In its conventional form, the jet algorithm combines the pair of clusters i, j with the minimum m_{ij}^2/W^2 to

be a ‘proto’ jet by adding the four-momenta p_i and p_j . This prescription is repeated iteratively for the remaining clusters and ‘proto’ jets until all possible combinations i, j lead to $m_{ij}^2/W^2 > y_{cut}$, the jet resolution parameter. In the present analysis, however, we use the jet algorithm to recombine the accepted clusters iteratively up to the point where exactly (2+1) jets remain. The smallest scaled jet mass given by any combination of the (2+1) jets is defined to be the observable y_2 . The y_2 distribution, $1/N_{DIS} dn/dy_2$, where N_{DIS} is the number of deep-inelastic scattering events passing the selection of Sect. 3, corresponds to the differential (2+1) jet event rate.

The same definition of the (2+1) jets and of the variable y_2 is used for the analysis of the data and of the Monte Carlo events after detector simulation. In events simulated at the hadron or parton level and in the NLO calculations, the jet algorithm is applied to hadron or parton four-momenta, respectively. The polar angle cut of 7° which is applied for clusters is also applied for hadrons, θ_{had} , and partons, θ_{par} . We take all components of the ‘missing momentum’ due to this cut into account and do not neglect the mass.

With these definitions we observe that the smallest mass m_{ij} of all possible combinations i, j of the (2+1) jets is most likely to be obtained by the combination of the two non-remnant jets. The fraction of events in which the minimum mass is formed by inclusion of the remnant jet is of the order of 15% for both data and NLO calculations.

In addition to the definition given above, we also measure the differential (2+1) jet rate and determine α_s using the E , E_0 and P variants of the JADE algorithm [17] without performing a full analysis of systematic errors. For these three algorithms m_{ij}^2 is defined as $(p_i + p_j)^2$. For the E algorithm, the combined four-momentum is simply the sum of the four-momenta $p_i + p_j$. For the E_0 algorithm, the combined energy is defined as $E_i + E_j$ and the combined momentum is $\frac{E_i + E_j}{|\mathbf{p}_i + \mathbf{p}_j|}(\mathbf{p}_i + \mathbf{p}_j)$. For the P algorithm, the combined momentum is $\mathbf{p}_i + \mathbf{p}_j$ and the combined energy is $|\mathbf{p}_i + \mathbf{p}_j|$. The definition of the recombination scheme for the latter two algorithms implies that the reconstructed jets are massless. This is not the case for the JADE algorithm and its E variant which conserve energy and momentum exactly in the recombination procedure.

5 Description of the data by QCD models

Before correcting the (2+1) jet event rate for detector and hadronization effects, as described in the next section, we study the description of the data by the QCD models LEPTO 6.5 and ARIADNE 4.08. LEPTO is based on the exact first order matrix elements followed by higher order radiation approximated by leading logarithm parton showers. In contrast, ARIADNE models the QCD cascade by emitting gluons from a chain of radiating colour dipoles. In QCD-Compton events the dipole is formed between the struck quark and the proton remnant, and the first gluon emission reproduces the first order matrix elements. In boson-gluon-fusion events, the quark and the

antiquark are generated according to the first order matrix elements. Two dipoles are formed between each quark and the proton remnant and continue to radiate independently. Both LEPTO and ARIADNE use the Lund string hadronization model [18]. We used the parameters of LEPTO and ARIADNE tuned to reproduce published HERA data [19], in combination with the parton density functions of MRSH [20]. The generated events were passed through a full simulation of the H1 detector. For each model an event sample was generated that was ~ 6 times larger than that of the experimental data. The same event and cluster cuts are applied to the simulated events as to the data.

In Fig. 1 we show the distributions of four representative jet variables: the differential (2+1) jet event rate y_2 , the variables z_p and x_p , and the polar angle of the most forward jet. The variable y_2 was defined above. The definitions of z_p and x_p are

$$z_p \equiv \min_{i=1,2} E_i (1 - \cos \theta_i) \bigg/ \sum_{i=1,2} E_i (1 - \cos \theta_i) \quad \text{and}$$

$$x_p \equiv \frac{Q^2}{Q^2 + m_{12}^2},$$

where E_i and θ_i are the energies and polar angles of the two non-remnant jets remaining after the clustering of the jet algorithm, and m_{12} is the corresponding invariant jet mass calculated without neglecting the jets’ masses. The variables x_p and z_p measure the approach to the (2+1) \rightarrow (1+1) singularities corresponding to the two non-remnant jets becoming one jet ($x_p \rightarrow 1$) or as one jet is absorbed into the remnant jet ($z_p \rightarrow 0$).

In order to increase the fraction of events with a clear (2+1) jet structure, thus enhancing the sensitivity to α_s , we define a subsample of 4503 events with $y_2 > 0.01$. To decrease the sensitivity to the modeling of initial-state multi-parton emissions and to avoid forward jets which are too close to the proton remnant, we further require that the non-remnant jets satisfy $10^\circ < \theta_{jet} < 145^\circ$. The requirement $\theta_{jet} > 10^\circ$ is found, in particular, to improve the description of the data by LEPTO. After these cuts, the (2+1) jet event sample consists of 2235 events.

In Fig. 1a the uncorrected y_2 data distribution is compared with the predictions of LEPTO and ARIADNE. The distribution is normalized to the total number of DIS events N_{DIS} selected in Sect. 3. Both models give an acceptable description of the data. At large values of y_2 , the distribution from ARIADNE tends to be above that of the data while LEPTO is systematically low. In Fig. 1b and c the z_p and x_p distribution are shown for uncorrected data and the models mentioned above. ARIADNE roughly describes the measured z_p distribution with the exception of the first bin, while LEPTO and data disagree in particular in the lowest two z_p bins. The poorest description of the data is observed for the x_p distribution. ARIADNE approximately reproduces the data in the central part of the distribution. It overestimates and underestimates the data in the very low and very high x_p region, respectively. LEPTO shows the opposite trend. Note that the drop of

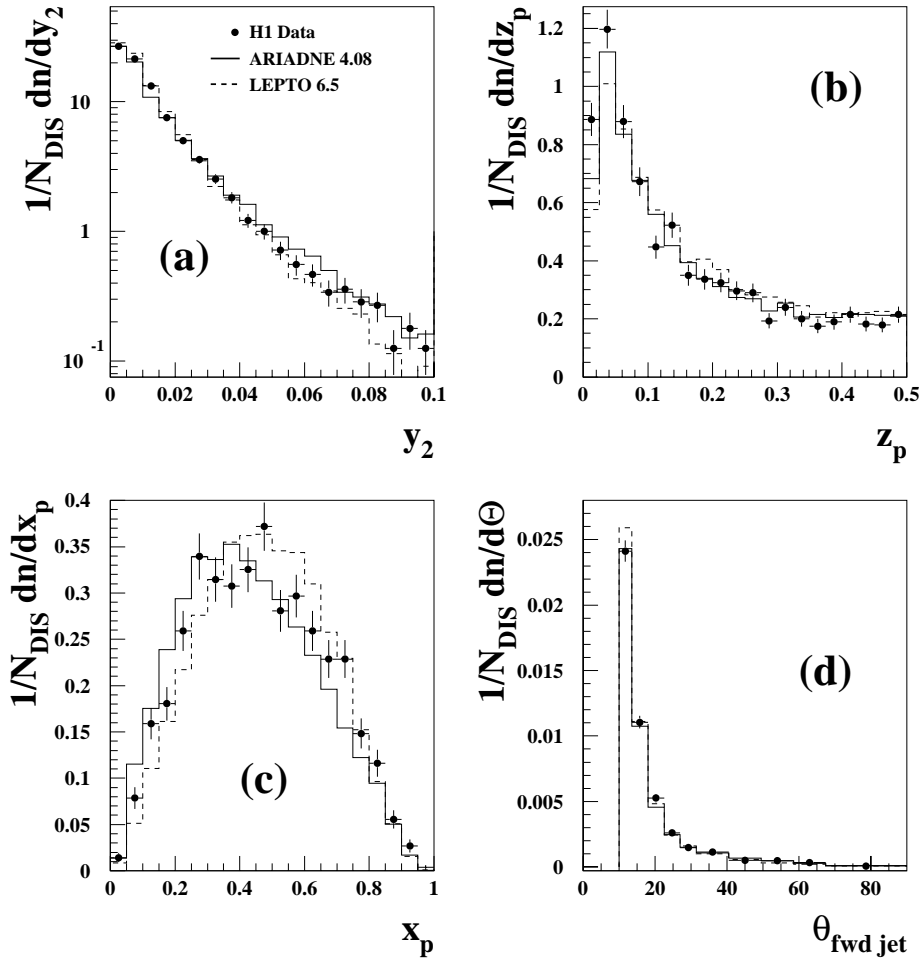


Fig. 1. Distributions of **a** y_2 , **b** z_p , **c** x_p and **d** the forward jet's polar angle $\theta_{fwd\,jet}$ for uncorrected data compared with the prediction of ARIADNE 4.08 and LEPTO 6.5 including full detector simulation. For all distributions the (2+1) jet event cuts $y_2 > 0.01$ and $10^\circ < \theta_{jet} < 145^\circ$ are applied with the exception of **a** where the cut $y_2 > 0.01$ is omitted. The distributions are normalized to the number of deep-inelastic events N_{DIS} passing the kinematic cuts. The errors are statistical only

the z_p distribution at the lowest z_p bin and the decrease of the x_p distribution at large values of x_p are consequences of the cut $y_2 > 0.01$. The distribution of the polar angle of the most forward non-remnant jet is shown in Fig. 1d. It is sharply peaked at small angles and is well described by both models.

We have studied the accuracy with which the data is described by ARIADNE and LEPTO for a wide range of selection criteria in addition to those discussed above. Overall ARIADNE gives the better description of the data. We conclude that the qualitative description of the data is acceptable and that a one-dimensional correction of the y_2 distribution is possible although an improved model description of the data is clearly desirable. In the following analysis, we correct the measured y_2 distribution with ARIADNE and use LEPTO as a consistency check.

6 Correction of the data

We correct the measured y_2 distribution by the method of regularized unfolding described in [21]. First, we unfold the y_2 distribution for detector effects only, in order to make direct comparisons with QCD model predictions

possible. For each simulated ARIADNE event, the value of y_2 is determined by clustering hadrons and simulated calorimeter clusters, respectively. Then, the y_2 distribution calculated from hadrons is reweighted such that the y_2 distribution from simulated clusters best fits the data. The weights are found by means of a log-likelihood method where strongly oscillating solutions are suppressed. As result, we obtain four bins of a reweighted y_2 distribution – corresponding to unfolded data. The unfolded distribution is given in Table 1. The quoted systematic error consists of two contributions added in quadrature: the influence of the uncertainty of the absolute hadronic energy scale of the liquid argon calorimeter, and the full difference to the y_2 distribution unfolded with LEPTO instead of ARIADNE. The unfolded y_2 distribution is shown in Fig. 2 together with the predictions of LEPTO and ARIADNE. The statistical error is of the order of 5% but the systematic errors can be larger. Both models roughly reproduce the data. The prediction of ARIADNE is high at large y_2 , while LEPTO falls too low. These observations are consistent with our conclusions from the comparison of the uncorrected data and the predictions of LEPTO and ARIADNE in Fig. 1.

Table 1. y_2 distribution determined with the JADE algorithm corrected for detector effects ($1/N_{DIS} dn/dy_2^{had}$), corrected for both detector and hadronization effects ($1/N_{DIS} dn/dy_2^{par}$), and the NLO prediction obtained from MEP-JET for $\alpha_s(M_Z^2) = 0.118$ in combination with the parton density functions MRSH ($1/\sigma_{DIS} d\sigma_{2+1}/dy_2$). All distributions are determined in the kinematic region defined in Sect. 3 and the cut $10^\circ < \theta_{jet} < 145^\circ$ is applied for hadron and parton jets, respectively. The first error is statistical, the second systematic. For the NLO calculation only the statistical error is given

y_2	$1/N_{DIS} dn/dy_2^{had}$	$1/N_{DIS} dn/dy_2^{par}$	$1/\sigma_{DIS} d\sigma_{2+1}/dy_2$
0.010 – 0.020	$13.43 \pm 0.49^{+0.45}_{-2.49}$	$15.06 \pm 0.87^{+0.44}_{-2.68}$	13.70 ± 0.15
0.020 – 0.035	$4.67 \pm 0.20^{+0.27}_{-0.51}$	$5.14 \pm 0.32^{+0.31}_{-0.53}$	5.01 ± 0.06
0.035 – 0.055	$1.51 \pm 0.08^{+0.33}_{-0.02}$	$1.71 \pm 0.12^{+0.15}_{-0.05}$	1.79 ± 0.03
0.055 – 0.100	$0.39 \pm 0.02^{+0.11}_{-0.01}$	$0.47 \pm 0.03^{+0.09}_{-0.03}$	0.53 ± 0.01

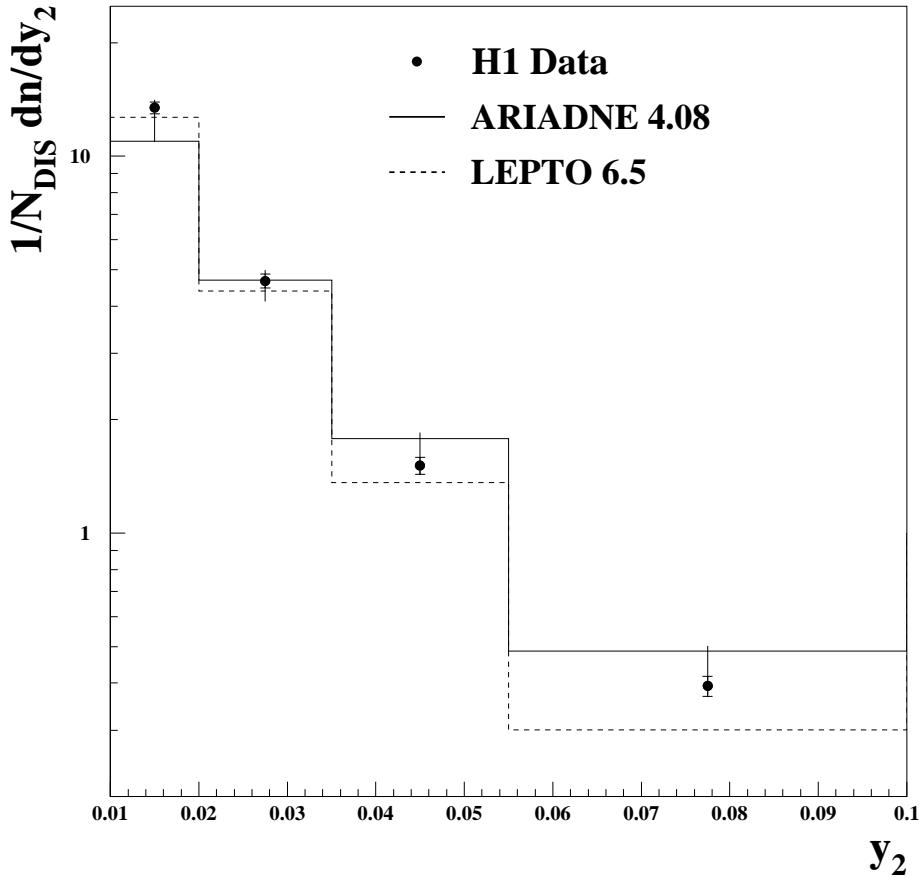


Fig. 2. Distribution of the observable y_2 corrected for detector effects compared with the prediction of the models ARIADNE 4.08 and LEPTO 6.5. As in Fig. 1, the cut $10^\circ < \theta_{jet} < 145^\circ$ is applied. The error bars correspond to the statistical and systematic errors added in quadrature. The inner error bars give the statistical error only

Next, we unfold both detector and hadronization effects in a one-step procedure in order to compare the data to NLO predictions. The unfolded distribution is also listed in Table 1 and is discussed in the next section. The size of the combined hadronization and detector migration is illustrated in Fig. 3 where the reconstructed y_2^{rec} after hadronization and detector simulation is compared with the y_2^{par} found by clustering the partons before hadronization. The bins shown correspond to those selected for the determination of α_s . For both LEPTO and ARIADNE a significant correlation is observed between y_2^{rec} and y_2^{par} . The y_2 distribution is systematically shifted to smaller y_2

values after hadronization and detector simulation, and the migrations are sizable. This is why a full unfolding procedure is used as opposed to a bin-by-bin correction factor method. It turns out that the results which were obtained using a bin-by-bin method are consistent with those from the unfolding procedure. We study the systematic uncertainty of the migrations in detail in Sect. 8 by using alternative QCD models for the correction of the data and by varying model parameters. We also compared distributions of other jet variables like x_p , z_p and jet polar angles for partons and for reconstructed clusters after

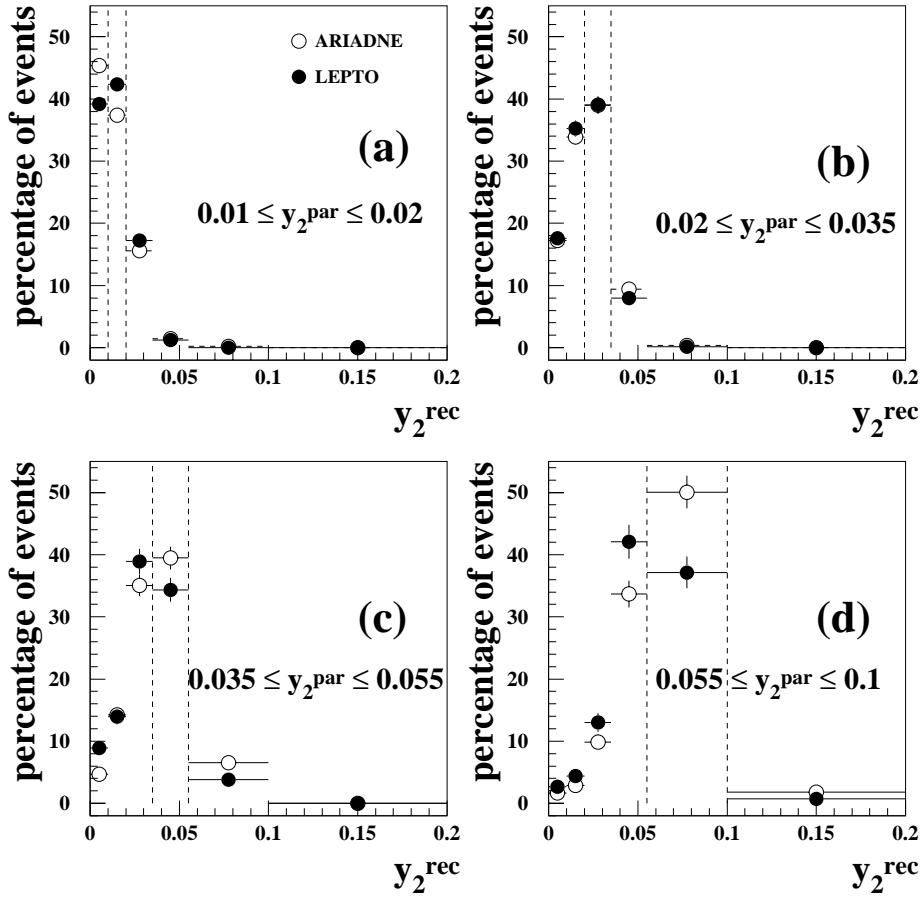


Fig. 3. **a** The distribution of y_2^{rec} as reconstructed from the calorimeter clusters after hadronization and detector simulation from the events with $0.01 < y_2^{par} < 0.02$ as predicted by ARIADNE 4.08 (white circles) and LEPTO 6.5 (full circles). The distribution is normalized to the number of events with y_2^{par} in the range $0.01 < y_2^{par} < 0.02$. **b**, **c** and **d** show the same for different ranges of y_2^{par} indicated by the legend and by the dashed vertical lines

hadronization and detector simulation. All the jet variables show clear correlations between the different levels.

7 NLO predictions and determination of α_s

7.1 NLO QCD programs

The NLO predictions are calculated with MEPJET, version 1.4 [8]. MEPJET allows arbitrary jet definitions and the application of cuts in terms of parton four-momenta. Other programs [22] were limited to a specific jet algorithm and made approximations in regions of phase space relevant for previous α_s analyses [2] that turned out to be imprecise [23]. MEPJET uses a ‘phase space slicing’ method [24] to deal with final-state infrared and collinear divergences associated with real emissions of partons. If the invariant mass squared s of a pair of partons in a multiparton state is smaller than a technical parameter s_{min} , soft and collinear approximations are applied to perform the phase space integrations analytically. The infrared and collinear divergences thus extracted cancel against those from the virtual corrections. If s exceeds s_{min} the integrations are done numerically without using explicit approximations.

We run MEPJET with s_{min} set to the recommended value of 0.1 GeV^2 . The statistical precision of the predicted y_2 distribution is $\sim 1\%$. As a cross check, we

changed s_{min} from 0.1 to 0.05 and 0.01 GeV^2 in MEPJET and observed no significant changes in the y_2 distributions. Note that our statistical precision at $s_{min} = 0.01 \text{ GeV}^2$ is then reduced to $\sim 2\%$ due to the larger fraction of (3+1) parton states treated numerically.

More recently the program DISENT [9] became available which uses a different technique to treat divergences based on a ‘subtraction’ method [25] in combination with dipole factorization theorems [26]. While we use MEPJET for this analysis, we have compared the predictions of MEPJET and DISENT version 0.1, which were run with the same value of $A_{MS}^{(4)}$ and the same parton densities, for all crucial distributions of this analysis and find general agreement at the level of a few percent. Looking to the y_2 distributions in detail, however, we see a significant discrepancy which is of little relevance for this analysis and is translated into an error in α_s in Sect. 8. To leading order we find the predictions of MEPJET and DISENT to be consistent within a fraction of a percent.

7.2 Comparison of QCD model and NLO predictions

Before extracting a value of α_s from a comparison of corrected data and NLO calculations, a region of jet phase space must be identified in which NLO predictions can provide a fair description of jet related observables. We verify the extent to which this is the case for the above

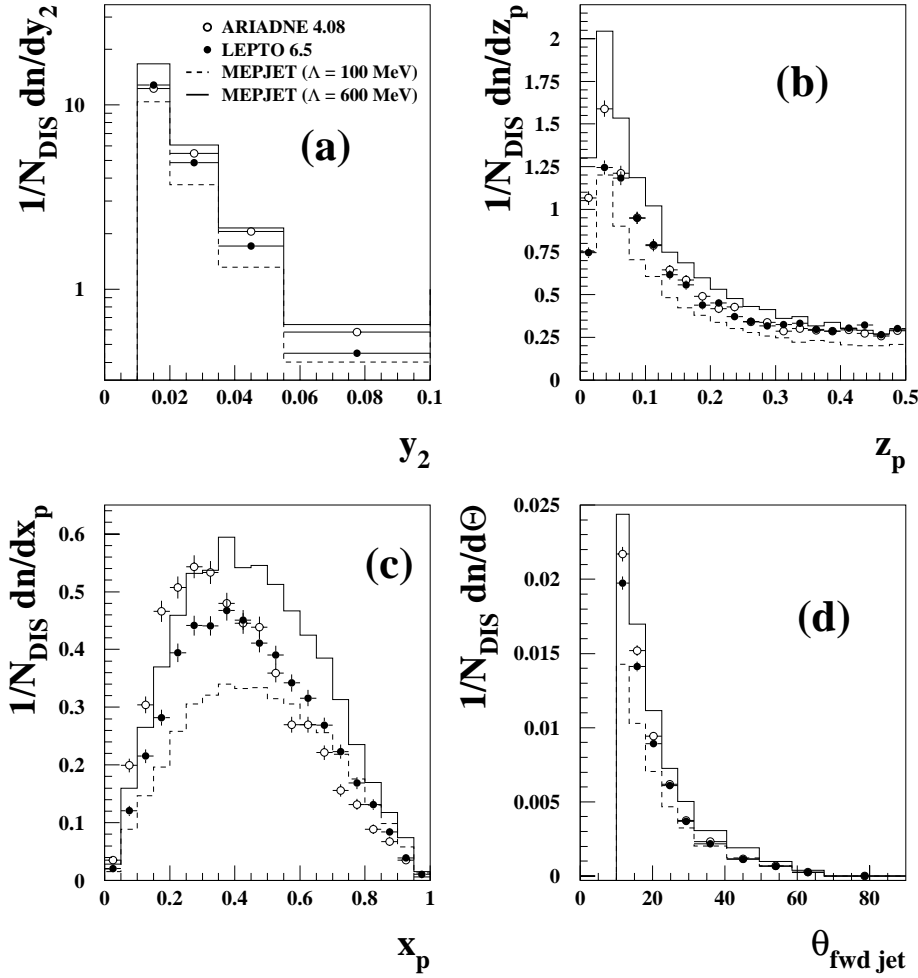


Fig. 4. NLO predictions based on MEPJET for the distribution of **a** y_2 , **b** z_p , **c** x_p and of **d** $\theta_{\text{fwd jet}}$ compared with parton jet distributions of ARIADNE 4.08 and LEPTO 6.5, respectively. The full line corresponds to MEPJET for the extreme value of $\Lambda_{\overline{MS}}^{(4)} = 600$ MeV and the dashed line to $\Lambda_{\overline{MS}}^{(4)} = 100$ MeV. The cuts $y_2 > 0.01$ and $10^\circ < \theta_{\text{jet}} < 145^\circ$ were applied for MEPJET, ARIADNE 4.08 and LEPTO 6.5 each

selections by comparing NLO jet distributions with the parton jet distributions of ARIADNE and LEPTO. The use of QCD model predictions rather than corrected data distributions gives reduced statistical error. In addition, the comparison of ARIADNE and LEPTO provides interesting information on possible ambiguities in the definition of the parton level to which the data are corrected.

In Fig. 4a the y_2 distributions for ARIADNE and LEPTO are shown together with NLO calculations for different values of $\Lambda_{\overline{MS}}^{(4)}$. In order to avoid a dependence of the following study on the value of α_s we chose the extreme values of $\Lambda_{\overline{MS}}^{(4)} = 100$ MeV and 600 MeV corresponding to $\alpha_s(M_Z^2) = 0.097$ and 0.132, respectively. (Note that $\Lambda_{\overline{MS}}^{(4)}$ serves only as a technical steering parameter for MEPJET.) The number of flavours used in the calculation is set at five. As with ARIADNE and LEPTO, the MRSH parton density functions are used in MEPJET. The same cuts on the hadronic final state, $y_2 > 0.01$ and $10^\circ < \theta_{\text{jet}} < 145^\circ$, that were applied for Fig. 1 are used here. Note that the mean number of partons per event with $\theta_{\text{par}} > 7^\circ$ is 9.7 for ARIADNE and 10.7 for LEPTO, whereas in MEPJET at most three partons and the proton remnant are produced.

We find that the distributions derived from ARIADNE and LEPTO are in qualitative agreement, and that their shapes are similar to those of the NLO distributions. However at larger values of y_2 , ARIADNE approaches the MEPJET prediction for $\Lambda_{\overline{MS}}^{(4)} = 600$ MeV, while LEPTO comes closer to the $\Lambda_{\overline{MS}}^{(4)} = 100$ MeV. This trend corresponds to that observed from the comparison of data and ARIADNE and LEPTO after detector simulation as shown in Fig. 1a.

The predictions of MEPJET and the distribution from ARIADNE for the z_p variable, shown in Fig. 4b, are also in fair agreement. LEPTO falls below ARIADNE at small z_p which is also seen in Fig. 1b. A pronounced difference between ARIADNE and NLO is seen in the x_p distributions shown in 4(c). This effect is not sensitive to changes of the phase space selection criteria and is further discussed in Sect. 8. The corresponding prediction of LEPTO agrees well with that of the NLO calculations. The distributions of the forward jet's polar angle from ARIADNE and LEPTO which are shown in Fig. 4d are well described in shape by QCD in NLO.

We conclude from this comparison that within the phase space region selected by the cuts listed above, NLO calculations are expected to provide an adequate descrip-

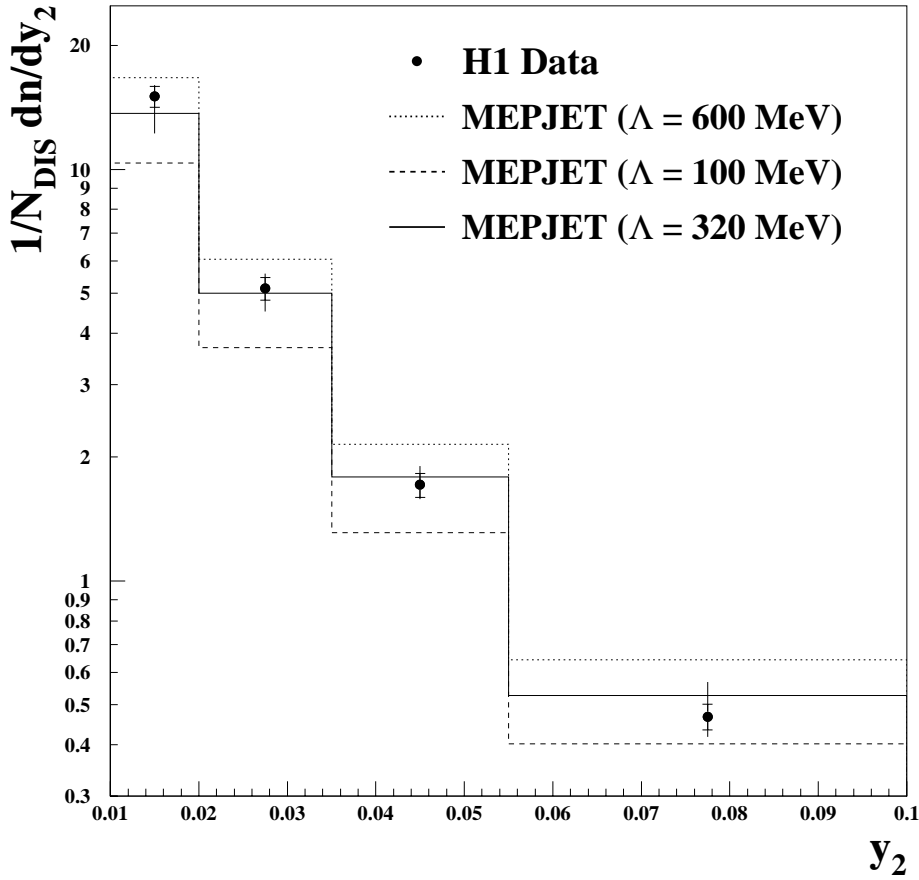


Fig. 5. Distribution of the differential jet rate y_2 corrected for detector and hadronization effects compared with the NLO prediction of MEPJET for $\Lambda_{\overline{MS}}^{(4)} = 600$ MeV (dotted line) and $\Lambda_{\overline{MS}}^{(4)} = 100$ MeV (dashed line). The full line shows the NLO prediction for the fitted value of α_s which corresponds to $\Lambda_{\overline{MS}}^{(4)} = 320$ MeV. The error bars on the corrected data distribution correspond to the statistical and systematic errors added in quadrature. The inner error bars give the statistical error only

tion of jet production in the data. This statement remains qualitative at this stage since we do not yet make an assumption on the value of α_s to be used in the NLO calculations and since we observe systematic differences between ARIADNE and LEPTO.

7.3 Fit of α_s

The y_2 data distribution corrected for detector and hadronization effects is compared with MEPJET in Fig. 5. For the first and last bin in particular the systematic error (see Sect. 8) is large compared with the statistical error and is dominated by the model dependence. The NLO predictions of MEPJET for different values of $\Lambda_{\overline{MS}}^{(4)}$ are also shown.

In NLO the differential jet rate is given by the expansion $1/\sigma_{DIS} d\sigma_{2+1}/dy_2 = A(y_2)\alpha_s + B(y_2)\alpha_s^2$. From the y_2 distributions in NLO, obtained by running MEPJET for $\Lambda_{\overline{MS}}^{(4)} = 100$ and 600 MeV, we obtain the coefficients A and B for the four bins in y_2 evaluating α_s at the scale $\mu^2 = \langle Q^2 \rangle$, where $\langle Q^2 \rangle \sim 620$ GeV² is the mean Q^2 of our (2+1) jet event sample. The mean Q^2 of the entire selected DIS event sample is 545 GeV².

In order to relate $\Lambda_{\overline{MS}}^{(4)}$ to $\Lambda_{\overline{MS}}^{(5)}$ and thus to α_s at a given scale μ^2 , we use the following formulae [27, 28]

$$\Lambda_{\overline{MS}}^{(5)} = \Lambda_{\overline{MS}}^{(4)} \left(\Lambda_{\overline{MS}}^{(4)} / m_b \right)^{2/23} \left[\ln \left(m_b^2 / \Lambda_{\overline{MS}}^{(4)2} \right) \right]^{-963/13225},$$

with m_b , the mass of the bottom quark, set to 5 GeV, and the two-loop expansion

$$\alpha_s(\mu^2) = \frac{4\pi}{\beta_0 \ln \left(\mu^2 / \Lambda_{\overline{MS}}^{(n_f)2} \right)} \times \left[1 - \frac{2\beta_1}{\beta_0^2} \frac{\ln \ln \left(\mu^2 / \Lambda_{\overline{MS}}^{(n_f)2} \right)}{\ln \left(\mu^2 / \Lambda_{\overline{MS}}^{(n_f)2} \right)} \right],$$

with $\beta_0 = 11 - \frac{2}{3}n_f$ and $\beta_1 = 51 - \frac{19}{3}n_f$, and n_f the number of quarks of mass less than μ , namely $n_f = 5$ in our case. The same formulae are used in the MEPJET program. Given A and B and the relation of $\Lambda_{\overline{MS}}^{(4)}$ to α_s , the NLO y_2 distribution can conveniently be calculated for any value of $\Lambda_{\overline{MS}}^{(4)}$.

We perform a minimum χ^2 fit ($\chi^2/d.o.f. = 6.9/3$) of $\Lambda_{\overline{MS}}^{(4)}$ taking into account the statistical correlations between the bins of the unfolded data distribution. As the result we obtain $\Lambda_{\overline{MS}}^{(4)} = 320 \pm 33$ MeV corresponding to $\alpha_s(M_Z^2) = 0.118 \pm 0.002$ (stat.). Note that the choice of $\mu^2 = \langle Q^2 \rangle$ for the calculation of the coefficients A and B is to some extent arbitrary. It influences the value of A and B but not the value of the fitted $\Lambda_{\overline{MS}}^{(4)}$. The NLO prediction corresponding to the fitted value of $\Lambda_{\overline{MS}}^{(4)}$ is shown

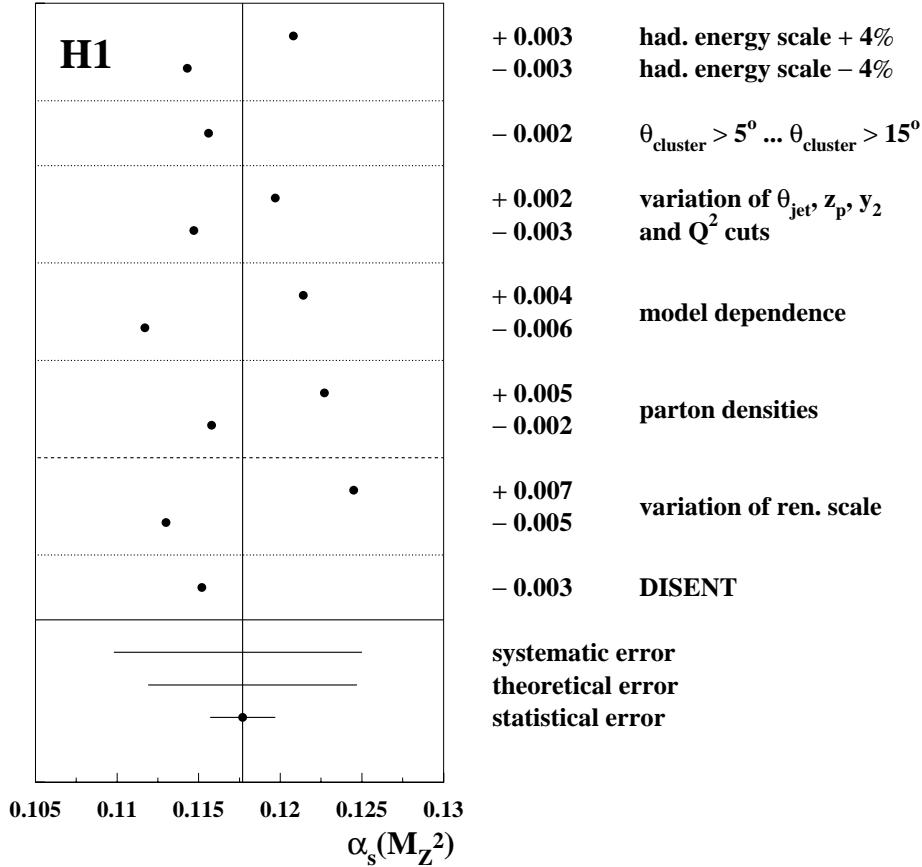


Fig. 6. List of systematic uncertainties on the fitted value of α_s . The horizontal lines separate different classes of uncertainties. The vertical line indicates the central value of $\alpha_s(M_Z)$ resulting from the fit. The black points give the values of α_s that are obtained when each source of systematic error is varied as described in the text. The uncertainties of the three classes below the dashed horizontal line are combined to give the theoretical error

as the full line in Fig. 5, and a good description of the data is observed.

8 Determination of systematic errors

We study various effects that might influence the result by varying the hadronic energy scale of the liquid argon calorimeter, changing the experimental cuts, and by using different Monte Carlo models for the data correction. We also use alternative parton density functions, measure jet rates with different variants of the modified JADE jet algorithm, and choose different renormalization and factorization scales. The various fitted values of α_s corresponding to different classes of uncertainties are shown in Fig. 6. All values of α_s given in the following refer to α_s at the scale $\mu^2 = M_Z^2$.

Energy calibration

The hadronic energy scale of the liquid argon calorimeter is varied by $\pm 4\%$ which leads to a systematic shift in y_2 . Note that there is no fully compensating effect in the ratio $y_2 = m_{ij}^2/W^2$ due to the definition of W which includes the ‘missing momentum’ vector. The resulting uncertainty in α_s is ± 0.003 .

The variation of the electromagnetic energy scale of $\pm 3\%$ leads to a negligible change in α_s .

Polar angle cuts $\theta_{clus}/\theta_{par}$

We vary the minimum value of the cluster acceptance cut θ_{clus} and in parallel the corresponding cut for partons θ_{par} within a range of $5^\circ - 15^\circ$. The variation of the $\theta_{clus}/\theta_{par}$ cut checks the quality of the detector simulation mostly but also the description of the data in the forward detector region where the models are less well tested. It also shows the stability of the proton remnant separation by the jet algorithm.

The additional α_s values fitted in this range of cluster cuts are slightly lower than the main value, the smallest one differing by -0.002 . We see no indication for a systematic trend in α_s as a function of the cut value. Without any cluster or parton cut the qualitative agreement between NLO and ARIADNE/LEPTO parton distributions deteriorates and stricter phase space cuts are needed. As an example we omit the cluster or parton cuts as well as the forward jets polar angle cut of 10° but apply the additional event cut $z_p > 0.15$. This reduces our (2+1) jet event sample by roughly a factor of 2. We obtain an α_s value of 0.119 ± 0.003 (*stat.*) which is consistent with our main result.

Event selection cuts

In addition to the $\theta_{clus}/\theta_{par}$ cut variation, we study the variation or introduction of various event cuts. As before,

all cuts are applied in parallel to quantities calculated from measured clusters, from simulated clusters and partons, and from the partons of the NLO program. We require $y_2 > 0.02$ instead of $y_2 > 0.01$. We change the polar angle jet acceptance cut to $\theta_{jet} > 8^\circ, 12^\circ$ or 14° . We require z_p to be larger than 0.05, 0.1 or 0.15. We unfold the differential jet rate for different Q^2 ranges and vary the minimum Q^2 cut from $Q^2 = 200 \text{ GeV}^2$ to $Q^2 = 100$ and 250 GeV^2 . Most of these variations correspond to significant changes in the number of events considered. However we find a variation of α_s of $+0.002$ and -0.003 at most. The largest change of -0.003 is found for the cut $y_2 > 0.02$. Note that the sizes of the observed changes in α_s are close to those of our statistical error, and that no indication of any systematic trend as a function of a cut variation is visible. Thus we regard the analysis as stable with respect to the phase space selection.

Model dependence

We test the model dependence of the result by repeating the analysis using LEPTO for the correction of the data. When using cuts identical to those given before, a value of $\alpha_s = 0.116$ is obtained. This result is reasonably stable with respect to the variation of $\theta_{clus}, \theta_{jet}, z_p$ and y_2 cuts, although the observed changes of the determined α_s values are larger than for the analysis based on ARIADNE.

Motivated by both the poor agreement of the shape of the x_p distributions between ARIADNE and NLO in Fig. 4c and the relatively large differences between the x_p distribution of data and ARIADNE in Fig. 1(c), we reweighted ARIADNE events such that the measured x_p distribution is reproduced. Effectively, this can be seen as a correction to the parton evolution mechanism of ARIADNE. This procedure leads to negligible change in the corrected y_2 data distribution but we find better agreement between ARIADNE and NLO in Fig. 4. Reweighting ARIADNE in x_p also gives a good description of the Q^2 dependence of the rate of (2+1) jet events, $R_{2+1}(Q^2) = N_{2+1}(Q^2)/N_{DIS}(Q^2)$, where ARIADNE (unweighted) was shown to be inferior to LEPTO [29].

Possibly large hadronization corrections could fake the radiation of hard partons described by perturbative QCD, and could cause systematic biases in the correction of the data. The uncertainty of the hadronization corrections is not directly tested by the comparison of LEPTO and ARIADNE since both models use the Lund string hadronization. We thus vary the parameters a and b of the Lund fragmentation function [18] and the parameter σ_q , which determines the mean p_t of a produced hadron, from their default values $a = 0.3$, $b = 0.58 \text{ GeV}^{-2}$ and $\sigma_q = 0.36 \text{ GeV}$, to $a = 0.1$ and 1.0 , $b = 0.44$ and 0.70 GeV^{-2} and to $\sigma_q = 0.25$ and 0.45 GeV . We derive hadronization correction factors for the y_2 distributions obtained from the events simulated with these sets of parameters. The differences between calculated correction factors do not exceed a few percent, and the corresponding variations in α_s which we find are at most $+0.002$ and -0.002 . In the same manner we vary the parameter Q_0 of LEPTO which cuts

off the evolution of the final state parton shower. Setting Q_0 to 4 instead of 1 GeV we observe a change of $+0.004$ in α_s . Setting the corresponding parameter for the initial state parton shower from 1.5 to 4 GeV, we observe a change of only 0.001 in α_s .

We repeat the analysis with the QCD model HERWIG, version 5.8 [30]. HERWIG combines a model for coherent parton shower radiation and an additional first order matrix element correction. Hadronization follows the cluster fragmentation model [31]. The description of the data with HERWIG is satisfactory for our purpose although HERWIG does not describe the y_2 distribution at very small y_2 and predicts the fraction of (2+1) jet events to be $\sim 10\%$ lower than that of the data. Unfolding the data with HERWIG leads to a change in the fitted α_s value of -0.006 . As result of the described variation of the models and of the model parameters we assess the total model dependence of our measurement to be $+0.004$ and -0.006 . The model dependence represents the main source of experimental uncertainty.

Parton density functions

The fit to the experimental y_2 distribution is repeated for several choices of parton density functions [32] in MEPJET including GRV HO (92), CTEQ2pM and CTEQ4M. We find a maximum variation of $+0.005$ and of -0.001 . This dependence is mostly due to the uncertainties in the gluon density function. Gluon-initiated processes account for $\sim 50\%$ of the (2+1) jet events in our sample.

Since we run MEPJET for values of $\Lambda_{\overline{MS}}^{(4)}$ different from those assumed during the global fits to deep-inelastic scattering data in which the parton density functions were determined, we study the effect of this inconsistency. This is done using the MRSA', MRSR and CTEQ4A series of parton density functions which each combine parton density functions determined on the basis of the same experimental data and the same fit procedure but with $\Lambda_{\overline{MS}}^{(4)}$ set to different values. From the observed change in the fitted value of α_s we estimate the effects of this inconsistency to be smaller than ± 0.002 . In total, we assign an uncertainty of $+0.005$ and -0.002 due to the knowledge of the parton density functions.

Different jet algorithms

In addition to the JADE algorithm, we determine α_s with three related cluster algorithms, namely the E , E_0 and the P algorithms. The unfolded differential jet rate distributions are given in Table 2.

Comparing the measured y_2 distributions for the JADE, E and P algorithms, we observe small but statistically significant differences. Similar differences are observed for the corresponding NLO predictions, which are given in Table 3, such that the fitted values of α_s do not differ much. We obtain $\alpha_s(M_Z^2) = 0.119 \pm 0.002$ and $\alpha_s(M_Z^2) = 0.117 \pm 0.002$ for the E and P algorithms, respectively.

Table 2. y_2 distribution corrected for both hadronization and detector effects for the E , E_0 and P algorithms. The error is statistical only

y_2^{par}	E	E_0	P
0.010 – 0.020	14.97 ± 0.79	15.14 ± 0.84	13.00 ± 0.76
0.020 – 0.035	6.59 ± 0.31	5.54 ± 0.32	4.66 ± 0.27
0.035 – 0.055	2.16 ± 0.13	1.76 ± 0.12	1.51 ± 0.10
0.055 – 0.100	0.63 ± 0.05	0.49 ± 0.03	0.42 ± 0.03

Table 3. NLO y_2 distribution obtained from MEPJET for the E , E_0 and P algorithms for the fitted values of $\alpha_s(M_Z^2) = 0.119, 0.120$ and 0.117 , respectively, in combination with the parton density functions MRSH

y_2^{NLO}	E	E_0	P
0.010 – 0.020	15.59 ± 0.15	14.27 ± 0.16	12.39 ± 0.15
0.020 – 0.035	5.67 ± 0.06	5.13 ± 0.06	4.42 ± 0.06
0.035 – 0.055	2.10 ± 0.03	1.85 ± 0.03	1.53 ± 0.03
0.055 – 0.100	0.66 ± 0.01	0.53 ± 0.01	0.46 ± 0.01

The measured y_2 distributions for the E_0 algorithm is closest to that for the JADE algorithm. To next-to-leading order these algorithms are identical. This is a consequence of the jet finders’ definitions and of the fact that in this analysis no cuts on the jets’ transverse (or longitudinal) momenta are made. The (small) difference in the measured y_2 distributions from these two algorithms may be interpreted as an expression of higher order recombination effects which cannot be accounted for in $O(\alpha_s^2)$ calculations. The value of α_s determined with the E_0 algorithm is $\alpha_s(M_Z^2) = 0.120 \pm 0.002$. The observed differences between the results of the different algorithms are small and are not treated as an additional error.

Renormalization and factorization scale

In NLO the y_2 distribution depends on the choice of the renormalization and factorization scales μ_r^2 and μ_f^2 . We estimate the renormalization scale dependence by varying μ_r^2 from Q^2 to $1/4 Q^2$ and $4 Q^2$ in MEPJET and by repeating the α_s fit. The corresponding uncertainty in α_s is $+0.007$ and -0.005 . In addition, we use the scalar sum of the transverse momenta of the jets in the hadronic centre-of-mass frame as a renormalization scale. This corresponds to a considerable difference in the magnitude of the renormalization scale given that Q^2 is typically about a factor of 20 larger than the square of a jet’s transverse momentum in the hadronic centre-of-mass frame. The corresponding change is close to that observed for $\mu_r^2 = 1/4 Q^2$.

In deep-inelastic scattering, collinear initial-state divergences are absorbed into redefined parton densities introducing the dependence on a factorization scale. We estimate the factorization scale dependence by varying μ_f^2 from Q^2 to $1/4 Q^2$ and $4 Q^2$ as we do for μ_r^2 , and we find the factorization scale dependence of α_s to be ± 0.001 .

DISENT NLO predictions

As an alternative to the determination of α_s based on MEPJET calculations we use DISENT predictions for the fit. The resulting change in α_s is -0.003 .

Discussion of higher order effects

This and similar analyses of e^+e^- annihilation data rely on the assumption that the distributions of observables obtained from NLO calculations and from the partons in the parton shower/colour-dipole models are comparable. There are, however, ambiguities in the definition of the parton level of the QCD models used to correct the data which can lead to uncertainties in the determined value of α_s . One may argue that the data should not be corrected to the level of the jets reconstructed from the final partons before hadronization but to that of the jets reconstructed from the partons at an earlier stage of the parton shower [33].

We study the dependence on the correction levels in two different ways. First, we investigate systematic changes of y_2 due to subsequent recombinations of partons during the dipole/parton shower radiation. We ‘pre’cluster the final partons of ARIADNE or LEPTO using $m_{ij}^2 = 2 \min(E_i^2, E_j^2) (1 - \cos \theta_{ij})$ as used in the Durham jet algorithm [17] and then continue clustering using the JADE definition. The ‘pre’clustering is stopped when the scaled invariant masses of all pairs of parton jets satisfy $m_{ij}^2/W^2 > 0.00005$, where m_{ij} is calculated according to the JADE definition. This corresponds to the point where on average (4+1) parton jets remain. We apply the JADE algorithm to these parton jets, continue clustering up to (2+1) jets and calculate y_2 . Comparing the result using this procedure with the y_2 distribution obtained using the JADE algorithm throughout, we see differences of a few percent for either ARIADNE or LEPTO. This translates into a similar difference of a few percent in the result for α_s . Larger differences are observed, however, when we extend the ‘pre’clustering further.

In the same spirit, we also change the value of the parameter Q_0 of LEPTO, which cuts off the final-state parton shower, as a means of looking at an early stage of the parton shower by forcing a change in the average number of partons produced. In contrast to the above variation of Q_0 in the context of the model dependence, here we are interested in the y_2 spectrum of a (variable) parton level keeping the hadron level fixed. We compare the differences in the y_2 distributions obtained. Again changes of a few percent are observed for e.g. $Q_0 = 3$ GeV instead of $Q_0 = 1$ GeV, but differences increase with larger values of Q_0 .

Note that the differences in the aforementioned definitions of the parton level may partially be due to unknown higher order corrections missing in NLO. The interpretation of these studies becomes difficult and we have not included such estimates in our combined error. Such effects might, in principle, be detected by comparing the shape of the distributions from NLO calculations and from parton

shower/colour-dipole models of Fig. 4. From another viewpoint differences in the measured α_s values using different jet recombination procedures, or a large dependence on the renormalization scale could be symptoms of the same difficulty. The dependence on the renormalization scale is the dominant uncertainty which is included in the systematic error. This situation with higher order effects and/or the ambiguity of the parton level is similar to that in e^+e^- annihilation [5] where such uncertainties turned out to be an important limitation.

Combined systematic error

We define the combined systematic error in the following way: assuming the errors of the different classes to be largely independent of each other, the positive and negative systematic errors of the first 5 classes are each added in quadrature. Thus we determine the systematic error of this analysis to be $+0.007$ and -0.008 . An additional theoretical error of $+0.007$ and -0.006 is obtained correspondingly, considering the measured difference between the JADE and E_0 algorithm, the renormalization scale uncertainty and the uncertainty due to observed difference of MEPJET and DISENT.

9 Summary

We have presented a measurement of jet related distributions in deep-inelastic scattering processes at HERA in the kinematic range $200 < Q^2 < 10\,000 \text{ GeV}^2$. The jets are found with the modified JADE jet algorithm. The measured jet distributions are compared with QCD model expectations and for most distributions we find acceptable agreement between the data and the models ARIADNE 4.08 and LEPTO 6.5. Acceptable agreement is also observed for the differential (2+1) jet event rate after correcting for detector effects.

The differential jet rate, corrected for both detector and hadronization effects, is compared with NLO QCD calculations in a region of jet phase space where the effect of higher-order parton emissions not considered in NLO is estimated to be small. A fit of the NLO predictions as a function of the strong coupling constant α_s is performed which results in

$$\alpha_s(M_Z^2) = 0.118 \pm 0.002 \text{ (stat.)}_{-0.008}^{+0.007} \text{ (syst.)}_{-0.006}^{+0.007} \text{ (theory)}.$$

A good description of the corrected differential jet rate by the next-to-leading order prediction is observed for the fitted value of α_s . The resulting α_s is compatible with previous α_s determinations based on the same observable in e^+e^- annihilation [5] and with the world average value of α_s [28] which provides a direct consistency check of perturbative QCD. The same conclusions are reached considering the results obtained with the E , E_0 and P variants of the modified JADE algorithm.

The most important uncertainties of the α_s value determined are caused by the as yet limited precision of the

data description by current QCD Monte Carlo models, by ambiguities in the definition of the parton level to which the data are corrected, and by the large renormalization scale dependence.

Acknowledgements. We are very grateful to the HERA machine group whose outstanding efforts made this experiment possible. We acknowledge the support of the DESY technical staff. We appreciate the big effort of the engineers and technicians who constructed and maintain the detector. We thank the funding agencies for financial support of this experiment. We wish to thank the DESY directorate for the support and hospitality extended to the non-DESY members of the collaboration.

References

1. H1 Collaboration, I. Abt et al., *Z. Phys. C* **61**, 59 (1994); ZEUS Collaboration, M. Derrick et al., *Z. Phys. C* **67**, 81 (1995)
2. H1 Collaboration, T. Ahmed et al., *Phys. Lett. B* **346**, 415 (1995); ZEUS Collaboration, M. Derrick et al., *Phys. Lett. B* **363**, 201 (1995)
3. JADE Collaboration, W. Bartel et al., *Z. Phys. C* **33**, 23 (1986); JADE Collaboration, S. Bethke et al., *Phys. Lett. B* **213**, 235 (1988)
4. See also K. Flamm, Doctorate Thesis, University of Hamburg, Germany, unpublished, 1996 and K. Flamm, Proc. of the Workshop ‘*DIS 96*’, Eds. G. D’Agostini, A. Nigro, 451
5. ALEPH Collaboration, D. Decamp et al., *Phys. Lett. B* **255**, 623 (1991); DELPHI Collaboration, P. Abreu et al., *Z. Phys. C* **54**, 55 (1992); OPAL Collaboration, P.D. Acton et al., *Z. Phys. C* **55**, 24 (1992); L3 Collaboration, O. Adriani et al., *Phys. Lett. B* **284**, 471 (1992); SLD Collaboration, K. Abe et al., *Phys. Rev. Lett.* **71**, 2528 (1993); For a recent review see: M. Schmelling, Proc. of ‘*ICHEP 96*’, Eds. Z. Ajduk, A.K. Wroblewski, World Scientific, (1997).
6. L. Lönnblad, *Comp. Phys. Comm.* **71**, 15 (1992)
7. G. Ingelman, LEPTO, version 6.1, Proc. of the Workshop ‘*Physics at HERA*’, Eds. W. Buchmüller, G. Ingelman, Vol. 3 (1992) 1366; G. Ingelman, A. Edin, J. Rathsmann, *Comp. Phys. Comm.* **101**, 108 (1997)
8. E. Mirkes, D. Zeppenfeld, *Phys. Lett. B* **380**, 205 (1996)
9. S. Catani, M.H. Seymour, *Nucl. Phys. B* **485**, 291 (1997)
10. H1 Collaboration, I. Abt et al., *Nucl. Instr. and Meth. A* **386**, 310 and 348 (1997)
11. H1 Calorimeter Group, B. Andrieu et al., *Nucl. Instr. and Meth. A* **336**, 499 (1993); H1 Calorimeter Group, B. Andrieu et al., *Nucl. Instr. and Meth. A* **350**, 57 (1994)
12. H1 Calorimeter Group, B. Andrieu et al., *Nucl. Instr. and Meth. A* **344**, 492 (1994)
13. DJANGO 6.2; G.A. Schuler, H. Spiesberger, Proc. of the Workshop ‘*Physics at HERA*’, Eds. W. Buchmüller, G. Ingelman, Vol. 3 (1991) 1419
14. S. Bentvelsen et al., Proc. of the Workshop ‘*Physics at HERA*’, Eds. W. Buchmüller, G. Ingelman, Vol. 1 (1991) 23; K.C. Höger, *ibid.* 43
15. H1 Collaboration, S. Aid et al., *Z. Phys. C* **67**, 565 (1995)
16. H1 Collaboration, T. Ahmed et al., *Nucl. Phys. B* **249**, 477 (1994)

17. S. Bethke et al., Nucl. Phys. B **370**, 310 (1992)
18. B. Andersson et al., Phys. Rep. **97**, 31 (1983); T. Sjöstrand, M. Bengtsson, Comp. Phys. Comm. **43**, 367 (1987)
19. N. Brook et al., Proc. of the Workshop 'Future Physics at HERA', Eds. G. Ingelman, A. de Roeck, R. Klanner, Vol. 1 (1995/96) 614
20. A.D. Martin, W.J. Stirling, R.G. Roberts, Proc. of the Workshop 'Quantum Field Theory and Theoretical Aspects of High Energy Physics', Eds. B. Geyer, E.M. Ilgenfritz, (1993) 11
21. V. Blobel, DESY 84-118, Dec. 1984 and Proc. of the 1984 CERN School of Computing, Aiguablava, Spain
22. J.G. Körner, E. Mirkes, G. Schuler, Int. J. Mod. Phys. A **4**, 1781 (1989); T. Brodtkorb, J.G. Körner, E. Mirkes, G. Schuler, Z. Phys. C **44**, 415 (1989); D. Graudenz, Phys. Lett. B **256**, 518 (1992); D. Graudenz, Phys. Rev. D **49**, 32591 (1994); D. Graudenz, CERN-TH.7420/94 (1994), to be published in Comp. Phys. Comm
23. See [8] and K. Rosenbauer, Proc. of the Workshop 'DIS 96', Eds. G. D' Agostini, A. Nigro, 444
24. K. Fabricius, G. Kramer, G. Schierholz, I. Schmitt, Z. Phys. C **11**, 315 (1982); W.T. Giele, E.W.N. Glover, Phys. Rev. D **46**, 1980 (1992)
25. R.K. Ellis, D.A. Ross, A.E. Terrano, Nucl. Phys. B **178**, 421 (1981); Z. Kunszt, D.E. Soper, Phys. Rev. D **46**, 192 (1992)
26. S. Catani, M.H. Seymour, Phys. Lett. B **378**, 287 (1996)
27. W. Marciano, Phys. Rev. D **29**, 580 (1984)
28. Particle Data Group, Phys. Rev. D **54** (1996), 77
29. F. Squinabol, Doctorate Thesis, University of Paris XI Orsay, France, unpublished, 1997; C. Niedzballa, Doctorate Thesis, RWTH Aachen, Germany, unpublished, 1997
30. G. Marchesini et al., Comput. Phys. Commun. **67** (1992), 465
31. B.R. Webber, Nucl. Phys. B **238**, 492 (1984)
32. M. Glück, E. Reya, A. Vogt, Z. Phys. C **53**, 127 (1992); CTEQ Collaboration, J. Botts et al., Phys. Lett. B **304**, 159 (1993); CTEQ Collaboration, J. Botts et al., MSUHEP-60426, CTEQ-604; A.D. Martin, R.G. Roberts, W.J. Stirling, Phys. Lett. B **356**, 89 (1995)
33. OPAL Collaboration, M.Z. Akrawy et al., Z. Phys. C **49**, 375 (1991)